

See discussions, stats, and author profiles for this publication at: <https://www.researchgate.net/publication/216584932>

Ligand-Centred Reactivity of Bis(picolyl)amine Iridium: Sequential Deprotonation, Oxidation and Oxygenation of a "Non-Innocent" Ligand

ARTICLE *in* CHEMISTRY - A EUROPEAN JOURNAL · NOVEMBER 2009

Impact Factor: 5.73 · DOI: 10.1002/chem.200901017

CITATIONS

29

READS

45

9 AUTHORS, INCLUDING:



Cristina Tejel

University of Zaragoza

92 PUBLICATIONS 1,478 CITATIONS

SEE PROFILE



Miguel Angel Ciriano

Spanish National Research Council

149 PUBLICATIONS 3,029 CITATIONS

SEE PROFILE



František Hartl

University of Reading

165 PUBLICATIONS 3,338 CITATIONS

SEE PROFILE



Bas de Bruin

University of Amsterdam

227 PUBLICATIONS 3,956 CITATIONS

SEE PROFILE

Ligand-Centred Reactivity of Bis(picolyl)amine Iridium: Sequential Deprotonation, Oxidation and Oxygenation of a “Non-Innocent” Ligand

Cristina Tejel,^{*,[a]} M. Pilar del Río,^[a] Miguel A. Ciriano,^[a] Eduard J. Reijerse,^[c] František Hartl,^[d] Stanislav Zális,^[e] Dennis G. H. Hetterscheid,^[b] Nearchos Tsiichlis i Spithas,^[b] and Bas de Bruin^{*,[b]}

Abstract: Treatment of $[\text{Ir}(\text{bpa})(\text{cod})]^+$ complex **[1]**⁺ with a strong base (e.g., $t\text{BuO}^-$) led to unexpected double deprotonation to form the anionic $[\text{Ir}(\text{bpa}-2\text{H})(\text{cod})]^-$ species **[3]**⁻, via the mono-deprotonated neutral amido complex $[\text{Ir}(\text{bpa}-\text{H})(\text{cod})]$ as an isolable intermediate. A certain degree of aromaticity of the obtained metal–chelate ring may explain the favourable

double deprotonation. The rhodium analogue **[4]**⁻ was prepared in situ. The new species $[\text{M}(\text{bpa}-2\text{H})(\text{cod})]^-$ (M = Rh, Ir) are best described as two-electron reduced analogues of the cationic

imine complexes $[\text{M}^{\text{I}}(\text{cod})(\text{Py}-\text{CH}_2-\text{N}=\text{CH}-\text{Py})]^+$. One-electron oxidation of **[3]**⁻ and **[4]**⁻ produced the ligand radical complexes **[3]**[•] and **[4]**[•]. Oxygenation of **[3]**⁻ with O_2 gave the neutral carboxamido complex $[\text{Ir}(\text{cod})(\text{py}-\text{CH}_2-\text{N}-\text{CO}-\text{py})]$ via the ligand radical complex **[3]**[•] as a detectable intermediate.

Keywords: bis(picolyl)amine • iridium • ligand radical • non-innocent ligands • oxygenation

Introduction

Over the past years we have become increasingly interested in the unusual chemistry of open-shell organometallic complexes of Rh and Ir.^[1] Such species reveal a rich chemistry, with several coupling and atom-abstraction reactions occurring at both the metal and ligand sites. While some of these

species should be regarded as “metallo-radicals”, others are better described as “ligand radicals” (Scheme 1). Generation of ligand radicals is expected for species with well-known redox active ligands such as catecholates/(semi)quinones^[2] and pyridine-2,6-diimines.^[3] We recently demonstrated that alkene ligands are also “redox non-innocent” when coordinated to the proper metal complexes.^[4] Amido ligands have also recently been demonstrated to be “redox non-innocent” by Grützmacher and co-workers in the presence of olefinic ligands.^[5]

Deprotonation of cationic $[\text{Rh}^{\text{I}}(\text{trop}_2\text{NH})(\text{bpy})]^+$ species (Scheme 1) generates neutral amido complex $[\text{Rh}^{\text{I}}(\text{trop}_2\text{N}^-)(\text{bpy})]$, which upon one-electron oxidation yielded $[\text{Rh}^{\text{I}}(\text{trop}_2\text{N}^\bullet)(\text{bpy})]^+$, the first stable and isolated transition-metal-coordinated aminyl radical instead of the expected Rh^{II} species.^[6] Although these aminyl radicals are stabilised by coordination to low-valent Rh and Ir centres, they still reveal controlled and interesting radical type behaviour. In an elegant bio-inspired approach, the substrate-binding properties of the metal were recently combined with the hydrogen-abstraction properties of the aminyl radical to arrive at new alcohol oxidation catalysts operating in a similar way as galactose oxidase.^[7]

Inspired by these results, we decided to investigate sequential deprotonation–oxidation reactions of our previously reported cationic $[\text{M}^{\text{I}}(\text{bpa})(\text{cod})]\text{PF}_6$ complexes (cod = *Z,Z*-1,5-cyclooctadiene; M = Rh, Ir),^[6a,8] aimed at generating

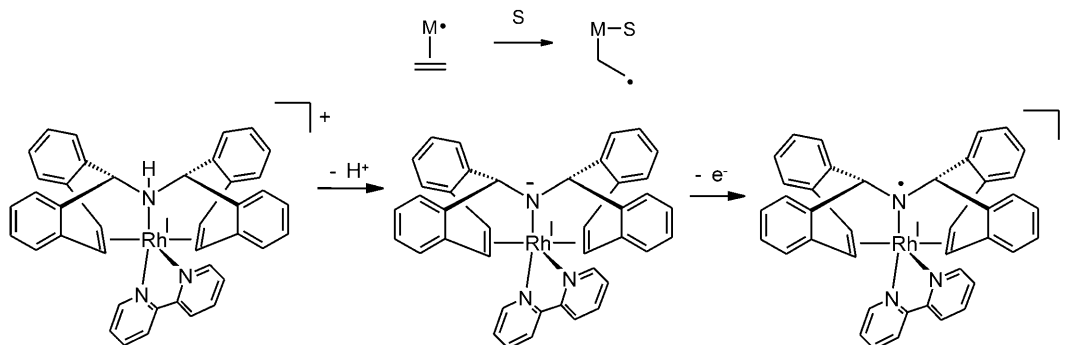
[a] Dr. C. Tejel, Dr. M. P. del Río, Prof. Dr. M. A. Ciriano
Instituto de Ciencia de materiales de Aragón (ICMA)
CSIC-Universidad de Zaragoza, Pedro Cerbuna 12
50007 Zaragoza (Spain)
Fax: (+34) 976-791187
E-mail: ctejel@unizar.es

[b] Dr. D. G. H. Hetterscheid, N. Tsiichlis i Spithas, Dr. B. de Bruin
Van 't Hoff Institute for Molecular Sciences (HIMS)
University of Amsterdam (UvA), Nieuwe Achtergracht 166
1018 WV Amsterdam (The Netherlands)
Fax: (+31) 20-525-5604
E-mail: b.debruin@uva.nl

[c] Dr. E. J. Reijerse
Max-Planck Institute for Bio-Inorganic Chemistry,
Stiftstrasse 34–36, 45470 Mülheim an der Ruhr (Germany)

[d] Prof. F. Hartl
University of Reading, Department of Chemistry
Whiteknights, PO Box 224, Reading RG6 6AD Berkshire (UK)

[e] Dr. S. Zális
J. Heyrovský Institute of Physical Chemistry
Academy of Sciences of the Czech Republic
Dolejškova 3, 182 23 Prague 8 (Czech Republic)



Scheme 1. "Redox non-innocent" behaviour of olefins and amido ligands

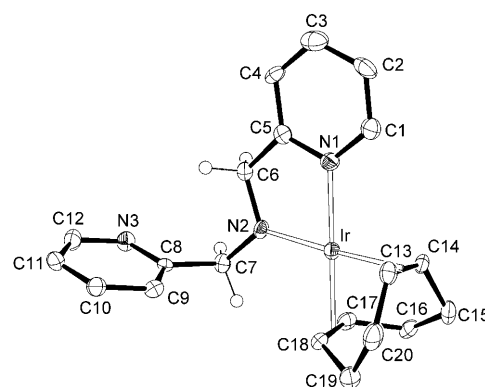
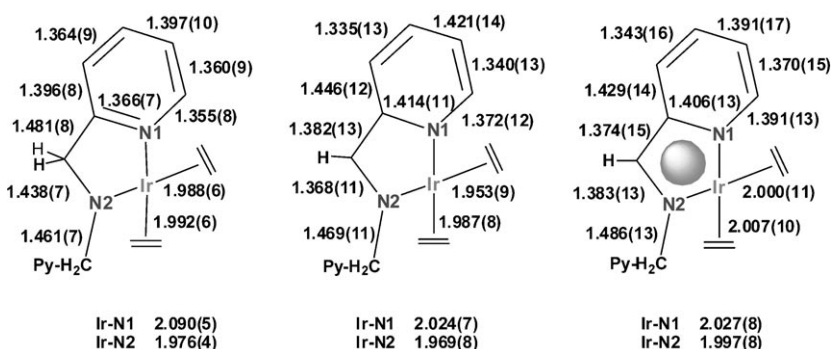
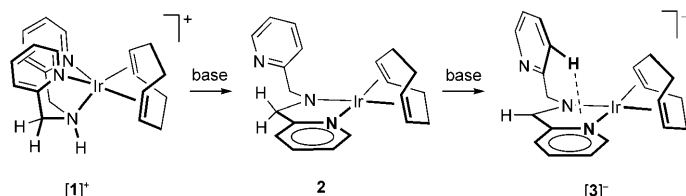
stable aminyl radical complexes. Much to our surprise, however, the deprotonation reactions led to unexpected double deprotonation of the bpa ligand ($\text{PyCH}_2\text{NHCH}_2\text{Py}$) with formation of unexpected complexes. The results are reported in this paper.

Results and Discussion

Treatment of the κ^3 -bpa pentacoordinated complex $[\text{Ir}(\text{bpa})\text{-(cod)}]\text{PF}_6$ (**1**) with 1 molar equiv of potassium *tert*-butoxide (KO^tBu) in THF resulted in a colour change from light yellow to deep red. ^1H NMR indicated the formation of the neutral amido complex $[\text{Ir}(\text{bpa-H})(\text{cod})]$ (**2**) as the main product, a consequence of the expected deprotonation of the bpa ligand at the amine nitrogen (Scheme 2). Late transition-metal amido complexes are not very abundant, but some somewhat related mononuclear pincer-type Ir^I-amido complexes were recently reported by Schneider et al.^[9]

On a preparative scale, complex **2** was smoothly isolated, in good yields, as a dark-red microcrystalline solid from the reaction of $[\text{Ir}(\mu\text{-OMe})(\text{cod})]_2$ with bpa (1:2) in toluene. The crystal structure of **2** is shown in Figure 1. Selected bond lengths are presented in Figure 2.

In the mononuclear complex **2**, the monoanionic bpa-H ligand chelates the iridium through the central amido nitro-

Figure 1. Structure (ORTEP at 50% level) of complex **2**.Figure 2. Selected experimental bond lengths [Å] of complex **2** (left), the anion of $\text{K}^*[\mathbf{3}]$ (middle) and $\text{K}^*[\mathbf{3}]$ (right). The sphere symbolises the encapsulated K^+ .Scheme 2. Formation of neutral **2** and anionic $[\mathbf{3}]^-$.

gen N2 and the N1 nitrogen of one of the pyridine rings. The iridium completes its approximately square-planar coordination with the diolefin ligand. The five-membered metal-lacycle was found to be almost planar (the maximum deviation of the plane defined by Ir, N1, C5, C6, N2 is 0.017 Å) and the amido N2 is strictly planar (sum of the angles around the nitrogen $\Sigma^0 = 360.1(4)^\circ$). The geometry around the amido N2 clearly reflects sp^2 hybridisation, thus suggesting some π interaction with iridium. Accordingly, the Ir-N2 distance is about 0.1 Å shorter than the related Ir-N1 one, and the Ir-Ct1 distance is slightly shorter than the related Ir-Ct2 distance (Ct1 and Ct2 are the centroids of the C13-C14 and C17-C18 bonds, respectively, see Figures 1 and 2).

The change from an Ir–N_{amine} to an Ir–N_{amido} bond enhances the electron density at iridium, and as a consequence, the iridium centre prefers to expel the other pyridyl arm of the bpa–H ligand, giving rise to the observed square-planar geometry. Moreover, the N2–CH₂ distances in and out of the metal chelate ring are slightly different (N2–C7: 1.461(7) and N2–C6: 1.438(7) Å), which could reflect some hyperconjugative effect on the methylene carbon (C6) of the metallacycle.

Figure 3 shows the packing of **2** in the crystal. Two molecules of **2**, related by an inversion centre, are forming a box-like dimer (Figure 3, top), leaving a distance between the parallel pyridyl planes of 3.598 Å. These dimers pack along the y axis to form an infinite π – π stacking array with a slightly shorter distance between the planes of the pyridyl rings (3.526 Å). Although these distances are typical for a π – π stacking interaction,^[10] these data alone are not enough to prove it.^[11]

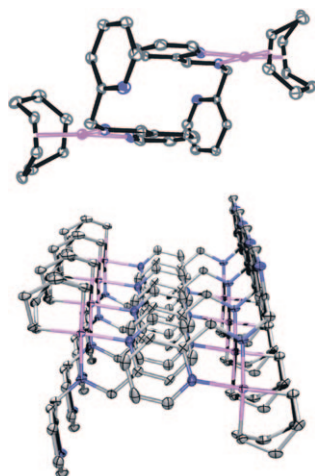


Figure 3. Top: Packing of complex **2** in box-like dimers. Bottom: Packing of complex **2** along the y axis.

The DFT (B3LYP, TZVP) optimised geometry of **2** is very similar to the X-ray structure. Attempts to optimise **2** with two coordinated pyridines led to pyridine dissociation of one of the pyridines, and the formation of square-planar **2**. The bond lengths and angles are close to those found in the X-ray structure (Figures 2, 4). The DFT calculated metal–ligand distances are slightly longer in the DFT geometry, but this is quite common for the B3LYP functional. In the DFT optimised geometry, the amido nitrogen is also planar (sum of the angles around the nitrogen $\Sigma^0 = 359.4^\circ$), and like in the X-ray structure, the Ir–N2 distance (2.029 Å)

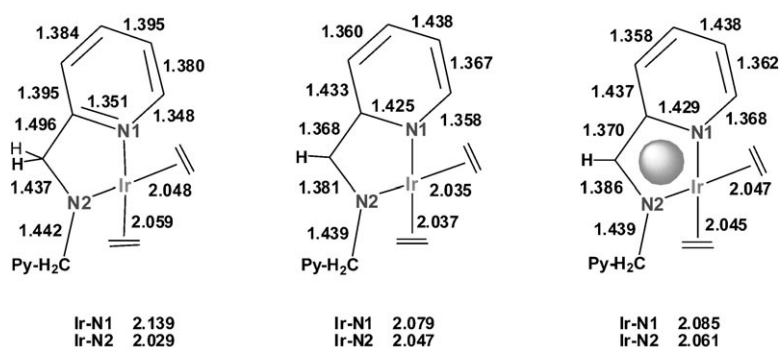


Figure 4. Selected distances in the DFT optimised (Turbomole, B3LYP, TZVP) complexes **2** (left), the free [3][–] anion (middle) and the potassium adduct K[3] (right). The sphere symbolises K⁺.

is shorter than the Ir–N1 distance (2.139 Å). At first sight, this behaviour is counterintuitive, because one might expect a repulsive interaction between the filled p orbital of the amido fragment and the filled Ir d orbitals (π conflict). This π conflict indeed exists in the HOMO of **2**, in which the N p orbital and an Ir d _{π} orbital show an antibonding interaction.

However, this repulsive interaction is counterbalanced by the increased π back-donation to the π^* orbital of the cod double bond *trans* to the amido fragment, thus resulting in some bonding character of the HOMO. The overall effect is a net π bonding between Ir and the amido fragment (Figure 5).

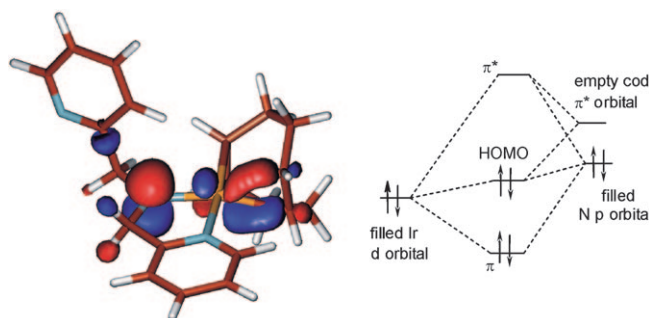


Figure 5. DFT calculated HOMO of **2**, and a simplified MO scheme explaining the net π -bonding between Ir and the amido fragment.

Quite surprisingly, a further reaction of complex **2** in THF with an additional molar equiv of KO^tBu, followed by the addition of the cryptand (4,7,13,16,21,24-hexaoxa-1,10-diazabicyclo[8.8.8]-hexacosane), produced the ionic complex [K(cryptand)][Ir(bpa–2H)(cod)] (K*[3]) through deprotonation of one of the methylene protons of the bpa–H ligand. Complex K*[3] was isolated as dark-red single crystals and fully characterised. The X-ray structure of the anion of K*[3] is shown in Figure 6. Selected bond lengths are shown in Figure 2.

Roughly, the geometries of anionic [3][–] and neutral **2** are quite similar, each X-ray structure showing a square-planar Ir(cod) fragment chelated by N1 and the central nitrogen N2. Closer inspection of the structures, however, clearly re-

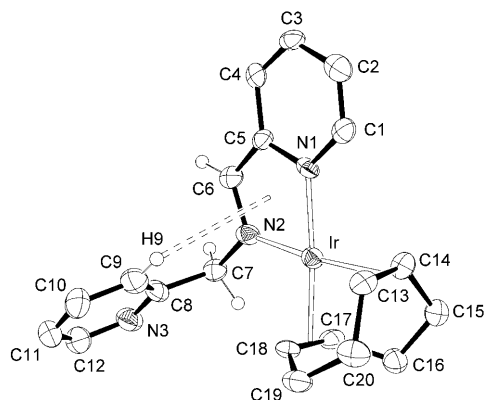


Figure 6. Structure (ORTEP at 50% level) of the anion of the complex $K^*[3]$.

veals the presence of the unexpectedly formed bpa-2H ligand. A cryptand-encapsulated K^+ serves as the counterion. Most pronounced changes on going from **2** to $[3]^-$ are observed within the five-membered metallacycle and the coordinated pyridyl ring (Figure 2). Thus, the significant shortening of the C5–C6 and C6–N2 distances in the metallacycle is accompanied by the shortening of the C1–C2 and C3–C4 distances in the coordinated pyridyl and shortening of the two Ir–N bonds. Both the C5–C6 and the C6–N2 distances are unusually short, suggesting a considerable double-bond character between these atoms, while within the coordinated pyridine ring, C1–C2 and C3–C4 seem to form two localised C=C bonds. This is indicated in Figure 2.

Interestingly, the uncoordinated pyridyl ring adopts a particular conformation (see Figure 7, left) in which the H9 proton is located close to the five-membered metallacycle. In order to facilitate the discussion, we will indicate this conformation as rotamer-0°. The distance of this proton to the centroid of the metallacycle (Ct3) is 3.042 Å while the angle C9–H9–Ct3 is 124.6°. Although this distance is quite long, this particular orientation of the ring suggests some C–H... π interaction according to the aromatic nature of the annulated ring structure constructed from the pyridyl fragment and the five-membered metallacycle ($4n+2$ Hückel system, $n=2$).

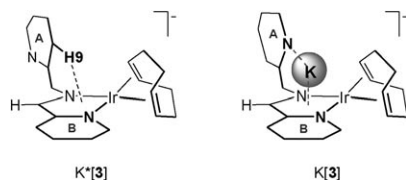


Figure 7. Observed interactions with the "aromatic" chelate ring of the anionic complexes $[3]^-$.

The DFT-optimised geometry of $[3]^-$ in $K^*[3]$ is very similar (Figure 4, middle), and the DFT calculations reveal comparable bond length changes on going from **2** to $[3]^-$. Also the orientation of the non-coordinating pyridyl ring is well

reproduced by the DFT calculations (Figure 8, left), where the distance of the H9 proton to the centroid of the metal chelate ring is shorter (2.810 Å) in the DFT geometry (C9–H9–Ct3 angle: 126.9°), suggesting that in the X-ray structure the C–H... π -interaction could be somewhat elongated by crystal packing forces.

In the absence of the cryptand, the dark-red solutions ob-

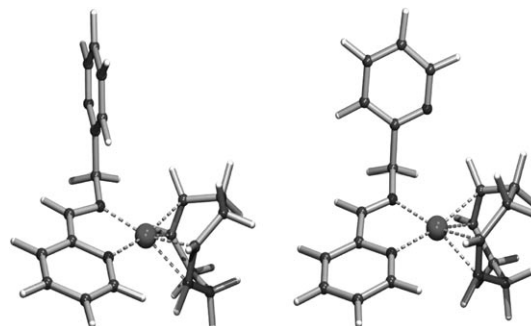
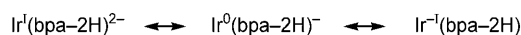


Figure 8. Optimised geometries of $[3]^-$ (left) and $[3]^+$ (right).

tained from the reaction of **2** and $KOtBu$, produced, after work-up, dark-red microcrystals of the previously communicated^[12] coordination polymeric chain $\{K[Ir(bpa-2H)(cod)]\}_n$ ($\{K[3]\}_n$). The most pronounced difference between $K^*[3]$ and $K[3]$ concerns the orientation of the non-coordinated pyridine ring (Py-A). Thus, while the orientation of the Py-A in $K^*[3]$ (Figure 7, left) corresponds to the rotamer-0°, it was found to be 180° rotated around the CH_2-C^{ipso} bond (rotamer-180°) in $K[3]$ (Figure 7, right). This conformer places N3 close to the metallacycle and in the appropriate orientation to form the cavity that encapsulates the K^+ cation.

The structural parameters commented above for the free anion in $K^*[3]$ point to a large contribution of the resonance structure in which a fully aromatic 10π electron $(bpa-2H)^{2-}$ ligand chelates iridium(I) in $[Ir^I(bpa-2H)^{2-}]$. However, the intrinsically non-innocent nature of this ligand type makes it feasible to consider the alternative $[Ir^{-I}(bpa-2H)]$ form (with a substantial Ir^{-I} π back-donation to the imine $(bpa-2H)$ after the "formal" transfer of two electrons from the bpa-2H ligand to the metal). Alternatively, a biradical description $[Ir^0(bpa-2H)^{\cdot-}]$ could be considered (Scheme 3).^[13] However, DFT calculations reveal that complex $[3]^-$ has a closed-shell singlet ground state (at both the BP86 and B3LYP levels).



Scheme 3. Resonance forms for the non-innocent $(bpa-2H)^{2-}$ ligand in $[3]^-$.

Attempts to optimise $[3]^-$ as an open-shell singlet (singlet biradical, broken symmetry approach) did not lead to a lower energy (the geometry converged to the same closed-shell singlet) and the optimised triplet configuration is 25 kcal mol⁻¹ higher in energy. Therefore, the electronic

structure of $[3]^-$ can only be described as a closed-shell singlet corresponding to the resonance forms $[\text{Ir}^{\text{I}}(\text{bpa}-2\text{H})^{2-}]$ and $[\text{Ir}^{\text{I}}(\text{bpa}-2\text{H})]$. The square-planar geometry around Ir suggests that the $[\text{Ir}^{\text{I}}(\text{bpa}-2\text{H})^{2-}]$ resonance form represents the largest contribution. Complex $[3]^-$ is thus best described as a two-electron-reduced analogue of the imine complex $[\text{Ir}^{\text{I}}(\text{cod})(\text{py}-\text{CH}_2-\text{N}=\text{CH}-\text{py})]^+$ ($[3]^+$). Therefore, to shed some more light on the electronic nature of $[3]^-$ we decided to optimise the geometry of $[3]^+$ with DFT, using the geometry of $[3]^-$ as input geometry.^[14] Quite remarkably, the optimisation cycles led the non-coordinating pyridine to rotate away from the metal chelate ring. Whereas in the optimised geometry of $[3]^-$ the pyridine clearly adopts the preferred rotamer-0° conformation indicative of an aromatic C-H $\cdots\pi$ -interaction, the non-coordinated pyridine in the optimised geometry of $[3]^+$ adopts the preferred rotamer-90° conformation (Figure 8). This suggests that the pyridyl annulated metal chelate ring of $[3]^-$ is indeed aromatic, while that of $[3]^+$ is non-aromatic (or Hückel anti-aromatic, with 8π electrons).

The elegant “cooperative (catalytic) reactions” recently reported by Milstein and co-workers, in which the metal and a reactive ligand site cooperate in substrate activation, are based on somewhat related late transition-metal complexes.^[15] In their case, however, single deprotonation at a benzylic position of the applied pyridine-based pincer complexes led to “dearomatisation” of the ligand.

In solution, complex $\text{K}^*[3]$ is a static species on the NMR time scale, producing sharp resonances in the ^1H and $^{13}\text{C}\{^1\text{H}\}$ NMR spectra (Figure 9). The most relevant features

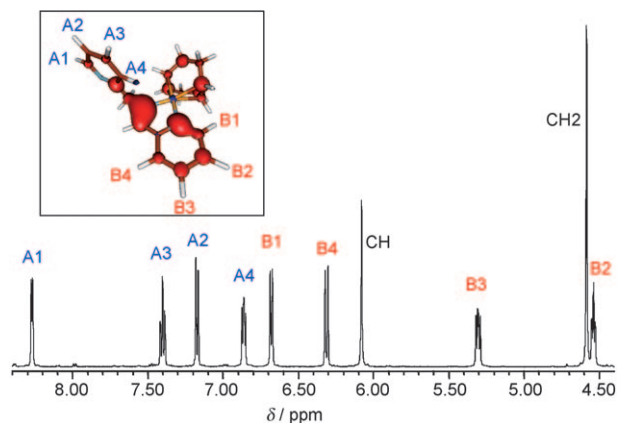


Figure 9. ^1H NMR and charge distribution (on the electrochemical potential) of the anion of $\text{K}^*[3]$ (blue is positive, red is negative).

of these spectra are the substantially upfield shifted signals corresponding to the coordinated pyridyl moiety, reflecting an increased electron density at this fragment closest to the deprotonated methylene unit. The negative charge of the dianionic bpa-2H ligand, introduced by the double deprotonation, is delocalised over the methine unit and, mainly, the B2 and B3 carbons of the adjacent pyridyl (Py-B), which, in turn, correspond to the most upfield shifted protons in

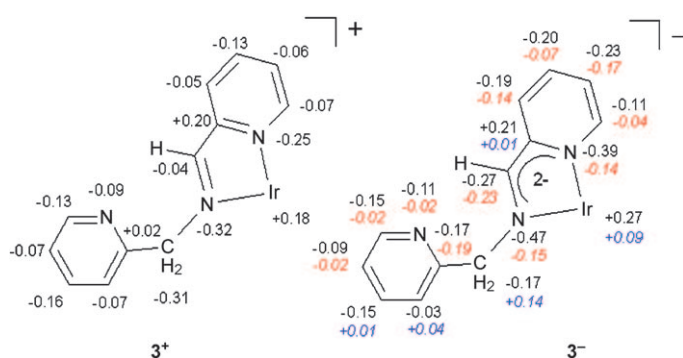


Figure 10. Mulliken charges distribution in $[3]^+$ (left) and $[3]^-$ (right). The values in red (negative) and blue (positive) are differences in Mulliken charges between $[3]^+$ and $[3]^-$ (B3LYP, TZVP).

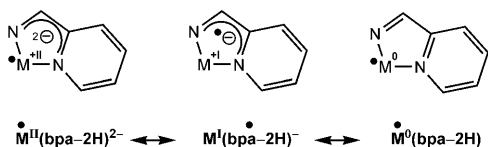
^1H NMR (Figure 9). A good correlation between the relative upfield ^1H NMR and ^{13}C NMR chemical shifts ($\Delta\delta$) of the coordinated py-B fragment of $[3]^-$ in the order $\text{B2} > \text{B3} > \text{B1} > \text{B4}$ with the relative DFT calculated Mulliken (Figure 10) charge density at the respective carbons is observed (Figure 9, inset).

Related rhodium complexes could not be isolated and just the anionic complex $\text{K}[\text{Rh}(\text{bpa}-2\text{H})(\text{cod})]$ ($\text{K}[4]^-$) was generated “in situ” by reacting $[\text{Rh}(\text{bpa})(\text{cod})]\text{PF}_6$ with two molar equiv of KO^tBu in THF, allowing its full characterisation in solution (see Experimental Section).

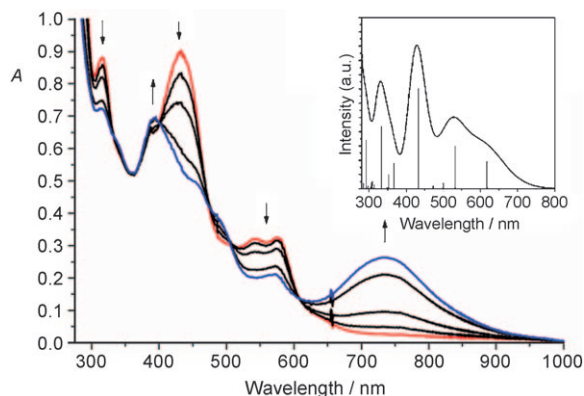
Ligand oxidation of $[3]^-$ and $[4]^-$ to form ligand radical complexes: The electronic structures of $[3]^-$ (Ir) and $[4]^-$ (Rh) comply with that of a doubly reduced α -diimine ($\text{RN}=\text{CR}'-\text{CR}'=\text{NR} + 2\text{e}^- \rightarrow \text{RN}^--\text{CR}'=\text{CR}'-\text{N}^--\text{R}$) complex,^[16] for which we can use the $\text{M}^{n+}(\text{L}^{2-})$ notation. Such ligands are strong π donors, and if the metal contains low-lying empty or half-filled d orbital(s), the alternative electronic structures $\text{M}^{(n-1)+}(\text{L}^-)$ or $\text{M}^{(n-2)+}(\text{L}^0)$ become accessible. It strongly depends on the mutual energy levels of the metal and ligand orbitals as for which assignment corresponds best to the actual electronic structure. Thus, these ligands are “redox non-innocent” and one should be careful in assigning oxidation states. 2,2'-Bipyridine and 1,10-phenanthroline type ligands can behave in a similar way. Formation of ligand radicals ($\text{L}^{\cdot-}$) upon reduction of late transition-metal complexes bearing such ligands has been described in a number of papers.^[17–20]

For the strongly delocalised closed-shell systems $[3]^-$ and $[4]^-$ the assignment of oxidation states and discrimination between relative contributions of the resonance forms $[\text{Ir}^{\text{I}}(\text{bpa}-2\text{H})^{2-}]$ and $[\text{Ir}^{\text{I}}(\text{bpa}-2\text{H})]$ is perhaps not very useful (see above). However, for their oxidised open-shell $S=1/2$ systems, the location of the unpaired electron (Figure 11) is in fact a measurable property. Since both the metal and the ligand in $[3]^-$ and $[4]^-$ are potential electron donors, we thus wondered what would happen upon oxidation of these species, and such we investigated their redox chemistry.

Cyclic voltammetry in THF reveals a reversible oxidation of $[3]^-$ at $E_{1/2} = -0.63$ V vs. Fc/Fc^+ (ferrocene/ferrocenium)

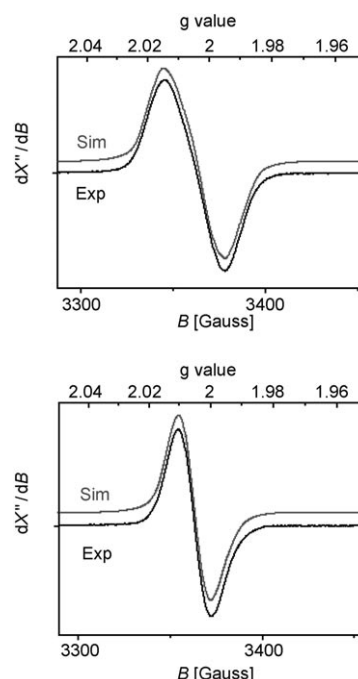
Figure 11. Resonance structures of $[3]^{\bullet}$ ($M=\text{Ir}$) and $[4]^{\bullet}$ ($M=\text{Rh}$).

at a scan rate of 100 mVs^{-1} .^[14,21] The one-electron-oxidised species $[3]^{\bullet}$ has a reasonable lifetime at room temperature, allowing its spectroscopic detection with UV/Vis spectroscopy. Clean formation of $[3]^{\bullet}$ is witnessed by observation of several UV/Vis isosbestic points upon electrochemical oxidation of $[3]^{-}$ in an OTTE cell (Figure 12). Direct reverse reduction of $[3]^{\bullet}$ resulted in a nearly full recovery of the original electronic absorption spectrum of $[3]^{-}$. A simultaneous reversible thin-layer voltammetric wave was recorded during the UV/Vis monitoring. Complex $[3]^{\bullet}$ slowly decomposes at room temperature in solution. Faster decomposition at higher concentrations indicates that the radical $[3]^{\bullet}$ dimer-

Figure 12. UV/Vis spectral changes accompanying electrochemical oxidation of $[3]^{-}$ (red line) to $[3]^{\bullet}$ (blue line). Conditions: THF/ $3 \times 10^{-4} \text{ M}$ Bu_4NPF_6 , room temperature, an OTTE cell. Inset: the simulated electronic absorption spectrum of 3^{\bullet} (Table 2) based on TD-DFT calculated excitation energies and oscillator strengths (represented by vertical lines).

ises or undergoes some other higher order decomposition pathway.

Chemical oxidation of $\text{K}[3]$ and $\text{K}[4]$ with one equivalent of AgPF_6 in THF, followed by rapid freezing, allowed us to detect the complexes $[3]^{\bullet}$ and $[4]^{\bullet}$ by means of EPR spectroscopy. The EPR spectra of the frozen solutions reveal almost isotropic signals with g values very close to g_e , suggesting that the unpaired electron of these species is mainly located at the bpa-like ligand (Figure 13). This assignment is in good agreement with the calculated (DFT) spin density distributions of $[3]^{\bullet}$ and $[4]^{\bullet}$ (Table 1). The unpaired electron is delocalised over the “imine” and “pyridine” fragments, but mainly resides at the “ α -diimine” fragment. Part of the spin density is also located at the C2 and C3 atoms of Py-B

Figure 13. Top: EPR spectrum of complex $[3]^{\bullet}$, freq. = 9.431943 GHz, $T = 20 \text{ K}$, att. = 30 dB, mod. amp. = 3 G. Bottom: EPR spectrum of complex $[4]^{\bullet}$, freq. = 9.438025 GHz, $T = 20 \text{ K}$, att. = 30 dB, mod. amp. = 3 G.Table 1. Experimental and calculated^[a] EPR properties of $[3]^{\bullet}$ and $[4]^{\bullet}$.

	g values (x,y,z)	A_M (x,y,z)	$A_N \text{ N2}$ (x,y,z)	$A_N \text{ N1}$ (x,y,z) (p_y)	$A_H \text{ CH}_2$ (x,y,z)	$A_H \text{ CH}$ (x,y,z)	$A_H \text{ B4}$ (x,y,z)	$A_H \text{ B3}$ (x,y,z)	$A_H \text{ B2}$ (x,y,z)	$A_H \text{ B1}$ (x,y,z)
$[3]^{\bullet}$	2.015 2.004	—	—	—	—	—	—	—	—	—
Exp	1.994	—	—	—	—	—	—	—	—	—
$[3]^{\bullet}$	2.016	−8.8	4.2	3.4	7.8, 4.0	−28.5	−5.1	−9.6	−14.5	−2.9
DFT	2.009	−8.3	4.4	3.6	8.2, 4.0	−19.5	−2.8	−6.9	−9.7	−0.8
	1.995	4.6	32.9	23.7	13.6, 9.5	−7.0	−0.5	−1.4	−3.1	0.8
$[4]^{\bullet}$	2.005	—	—	—	9.1, 5.3	−26.8	−4.2	−8.7	−14.2	−2.5
Exp	2.001	—	—	—	9.5, 5.4	−18.2	−2.0	−6.2	−9.1	−0.1
	1.997	—	—	—	15.1, 11.1	−6.0	+0.3	−0.7	−2.3	1.1
$[4]^{\bullet}$	2.006	4.8	4.7	3.7	9.1, 4.3	−27.4	−5.0	−9.3	−15.2	−2.5
DFT	2.005	4.5	5.0	3.8	9.5, 4.4	−18.8	−2.8	−6.8	−10.1	−0.1
	2.001	1.3	35.8	24.8	15.1, 10.1	−6.6	−0.5	−1.3	−3.3	1.1

[a] ADF, BP86, TZP. Hyperfine couplings in MHz.

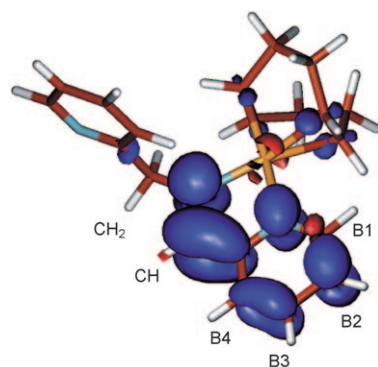


Figure 14. Spin density plot of complex $[3]^\bullet$ (Turbomole B3LYP, TZVP level). The spin distribution in $[4]^\bullet$ is similar.

(Figure 14). There is virtually no spin density at the metal, and thus $[3]^\bullet$ and $[4]^\bullet$ are best described by their $[M^I\{(bpa-2H)^\bullet\}]$ resonance structures (Figure 11, middle).

The experimental EPR spectra are rather broad and do not reveal any resolved hyperfine couplings. To validate the assignment of the electronic structures of $[3]^\bullet$ and $[4]^\bullet$ we calculated the spectral properties with DFT. The results are shown in Table 1. The experimental X-band EPR signal of complex $[4]^\bullet$ could in principle be simulated with isotropic g values, but a clearly better agreement between the experimental and simulated line-shapes was obtained by assuming a slightly rhombic g tensor, with $g_x=2.005$, $g_y=2.001$ and $g_z=1.997$. Indeed, this rhombicity is resolved at Q band. The rhombicity of the g tensor is already resolved in the X-band EPR spectrum of $[3]^\bullet$, which could not be simulated with isotropic g values. A satisfactory simulation required a rhombic g tensor, with $g_x=2.015$, $g_y=2.004$ and $g_z=1.994$ (Figure 13). These values are in excellent agreement with the values obtained with DFT (Table 1).

Although the experimental spectrum does not reveal any resolved hyperfine couplings, the inclusion of some hyperfine couplings in the simulations made it easier to simulate the experimental line-shape. Based on the DFT values in Table 1, we included hyperfine couplings with two equivalent nitrogen nuclei along g_z ($A_z^{2N} \sim 25$ MHz), iridium ($A_x^{\text{Ir}}=A_y^{\text{Ir}} \sim 9$, $A_z^{\text{Ir}} \sim 5$) and a proton along g_x and g_y ($A_x^{\text{H}}=A_y^{\text{H}} \sim 20$), which gave satisfactory results (Figure 13). The pulse ENDOR spectrum of $[4]^\bullet$ (Figure 15) revealed at least four distinct ^1H hyperfine couplings. Due to the many overlapping signals the spectrum did not contain enough information for independent simulation of all protons. A set of coupling parameters based on the DFT calculations in which only the isotropic part of the hyperfine tensors was slightly modified (Table 1) gave a quite satisfactory simu-

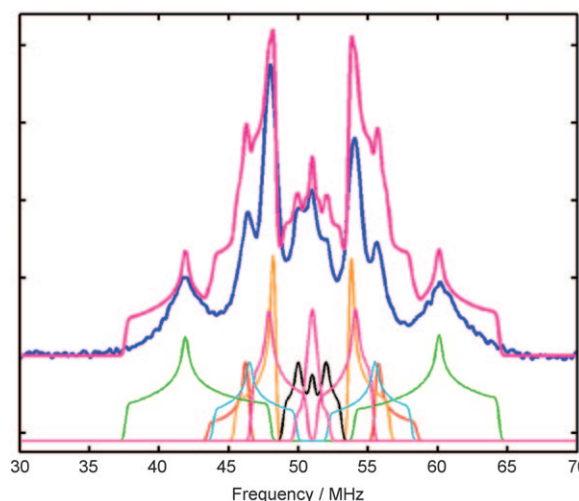


Figure 15. ^1H Davies ENDOR at Q-band (33.5308 GHz) of $[4]^\bullet$ (blue trace). Experimental conditions: 20 K, Field 1197.5 mT, $t_{\text{RF}} = 18 \mu\text{s}$. Simulation parameters (pink trace) are listed in Table 1. The individual contributions to the ENDOR spectrum are drawn below the experimental and simulated spectrum.

Table 2. TD-DFT calculated excitation energies (E) for $[3]^\bullet$ with oscillator strength (O.S.) larger than 0.03.

State	Main contribution	Calcd ^[a] (E [eV]) ^[c]	O. S.	Exptl ^[a,b] (E [eV]) ^[c]
^2A	SOMO (α) \rightarrow LUMO (α)	1.94 (639)	0.020	1.56 (738)
^2A	HOMO-1(β) \rightarrow LUMO(β)	2.74 (453)	0.053	2.53 (490)
^2A	(SOMO \rightarrow LUMO+2)	2.89 (429)	0.056	2.73 (455)
^2A	(HOMO-3 \rightarrow SOMO)	3.36 (369)	0.142	3.15 (393)
^2A	mixed	3.84 (323)	0.080	3.78 (328)

[a] See Figure 16. [b] THF/ $3 \times 10^{-1} \text{ M}$ Bu₄NPF₆, room temperature. [c] The corresponding value of λ_{max} [nm] in brackets.

tion (Figure 15). The relaxation times of $[3]^\bullet$ were unfavourable for a successful ENDOR experiment.

TD-DFT calculations reproduced appreciably well the experimental electronic absorption spectrum of $[3]^\bullet$ (Table 2, Figure 12, inset). The majority of intense absorption features in the UV/Vis spectrum correspond to the electronic excitations originating in the “imine”-localised HOMO. The lowest-energy transition is (bpa-2H)-intraligand (IL) in nature, having a dominant contribution from the HOMO to the (non-coordinated) pyridyl-localised LUMO (Figure 16). The dominant transition in the visible part of the spectrum at 431 nm, HOMO to LUMO+4, can be assigned to have a mixed IL and LMCT character.

The experimental electronic absorption spectrum of the open-shell radical complex $[3]^\bullet$ is less precisely fitted by the TD-DFT calculations (Table 3, Figure 17). Nevertheless, the qualitative differences in both spectra are well reproduced.

The calculations indicate the shift of the lowest-lying intraligand transition to a longer wavelength. The most intense electronic transition in the visible region, HOMO-3 to SOMO (in $[3]^\bullet$ having a mixed MLCT and IL character), is correctly calculated at a higher energy than in the case of $[3]^-$ (Tables 2 and 3). The LUMO(α) of $[3]^\bullet$ has a different character than the LUMO of $[3]^-$, being localised largely on

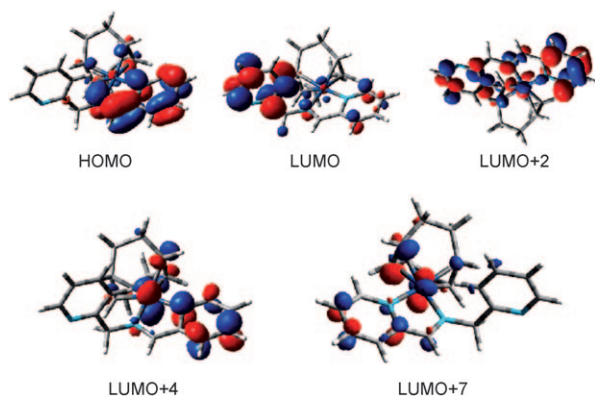


Figure 16. Molecular orbitals of $[3]^-$ involved in the significant UV/Vis electronic transitions (Table 2).

Table 3. TD-DFT calculated excitation energies (E) for $[3]^+$ with oscillator strength (O.S.) larger than 0.02.

State	Main contribution	Calcd ^[a] (E [eV]) ^[c]	O. S.	Exptl ^[a,b] (E [eV]) ^[c]
b^1A	HOMO \rightarrow LUMO	2.02 (614)	0.037	2.14 (578)
c^1A	HOMO \rightarrow LUMO + 2	2.35 (528)	0.059	2.29 (542)
$f^1[a]$	HOMO \rightarrow LUMO + 4	2.89 (429)	0.137	2.88 (431)
$g^1[a]$	HOMO \rightarrow LUMO + 5	3.43 (362)	0.035	3.67 (338 sh)
$i^1[a]$	HOMO \rightarrow LUMO + 7	3.78 (328)	0.086	3.91 (317)

[a] See Figure 17. [b] THF/ 3×10^{-1} M Bu_4NPF_6 , room temperature. [c] the corresponding value of λ_{max} (nm) in brackets.

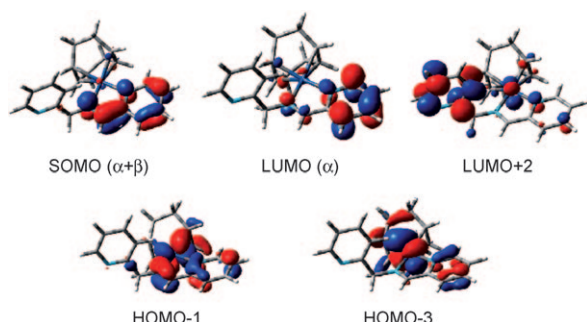


Figure 17. Molecular orbitals of $[3]^+$ involved in the significant UV/Vis electronic transitions (Table 3, Figure 12). The higher lying LUMO (β) (not shown) is very similar to SOMO (α) (shown).

the coordinated pyridyl moiety of the *bpa*-2H ligand instead of the free one in the case of $[3]^-$. The largely (*bpa*-2H)-based LUMO(α) of $[3]^+$ is therefore related to the LUMO+4 of $[3]^-$, although the metal contribution in the latter orbital is significant. The stabilisation of this orbital upon the oxidation of $[3]^-$ to $[3]^+$ is proposed to result in the large red shift of the intense visible band at 429 nm in the experimental UV/Vis spectrum of $[3]^-$ to 738 nm in $[3]^+$ (Figure 12).

The DFT calculations have further revealed some marked bond-length changes upon one-electron oxidation of $[3]^-$ to $[3]^+$, with longer Ir–N distances and less explicit bond-length equalisation within the chelate ligand part (shorter C–N bonds, longer C–C bond), pointing to a decreased “aromaticity” of the annulated metal–chelate ring in $[3]^+$ (see Figure 18). In good agreement with this interpretation, the

distance between the H9 proton and the centroid of the metal chelate ring becomes substantially longer upon one-electron oxidation of $[3]^-$ (2.810 Å) to $[3]^+$ (2.930 Å). On the other hand, some of these bond-length changes within the chelate ligand part are also expected on the basis of the different resonance structures of $[3]^-$ - $\{Ir^I(bpa-2H)^{2-}\}$ and $[3]^+$ - $\{Ir^I(bpa-2H)^+\}$.

Mono-oxygenation of the *bpa*-2H ligand via radical species $[3]^+$

Treatment of THF solutions of $K[3]$ with O_2 led to formation of the carboxamido complex $[Ir(bpam-H)(cod)]$ (**5**) in approx. 60 % yield (based on NMR spectra with an internal standard), see Scheme 4.

The identity of **5** was confirmed by its independent synthesis from the preformed *bpam* ligand (*bpam* = *N*-(2-picolyl)picolinamide) and $[Ir(\mu-OMe)(cod)]_2$ (1:2), which led to the selective formation of **5** as a single isomer. The X-ray structure of **5** is depicted in Figure 19.

Coordination of the *bpam*-H ligand to iridium in **5** occurs through the amido nitrogen (N2) and the nitrogen

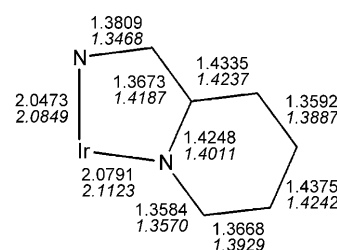
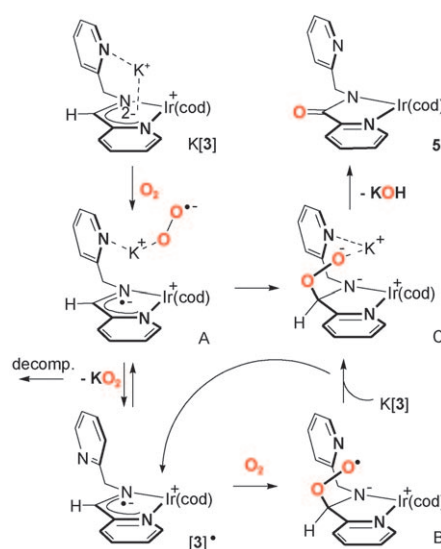


Figure 18. Selected bond lengths [Å] in $[3]^-$ and $[3]^+$ (in italics) from DFT calculations.



Scheme 4. Proposed mechanism for formation of **5** from $K[3]$.

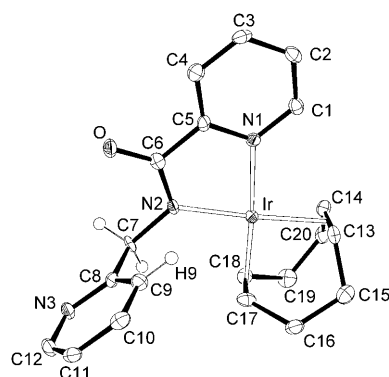


Figure 19. Structure (ORTEP at 50% level) of complex **5**.

(N1) of the carbonyl-bound pyridyl ring. The square planar coordination geometry around iridium is completed by the chelating cod ligand. The Ir–N_{py} (N1) distance [2.088(3) Å for the second independent molecule in the unit cell] is similar to that in **2** while the Ir–N_{amido} (N2) distance [2.041(3) [2.046(3) Å]] is slightly longer than that in **2**.

The transformation of the bpa–2H ligand of [3][−] into the carboxamido ligand bpam in **5** within the reactive electron rich and unsaturated coordination sphere of iridium, without oxidation of the Ir^I(cod) fragment is noteworthy. In many cases, Ir^I(cod) fragments supported by N-donor ligands are easily oxygenated.^[22] The coordination of K⁺ to the anion [3][−] seems to be important for the selectivity in the reaction with O₂, since K⁺[3] (having the K⁺ ion encapsulated by the cryptant) reacts much less selectively with O₂, producing a rather complex mixture of yet unidentified species.

The formation of **5** proceeds via the ligand radical complex [3][•] as a clearly detectable intermediate, as revealed by EPR spectroscopy. Exposure of a THF solution of K[3] to air, followed by rapid freezing of the mixture in liquid N₂, gives rise to the characteristic EPR signal of [3][•] in the initial stages of the reaction (the reaction proceeds at room temperature). Upon prolonged exposure of the solution to air at room temperature, the signal of [3][•] gradually disappears (Figure 20).

We therefore propose a mechanism as depicted in Scheme 4 for the formation of complex **5** through mono-oxygenation of K[3] by O₂. One-electron oxidation of [3][−]

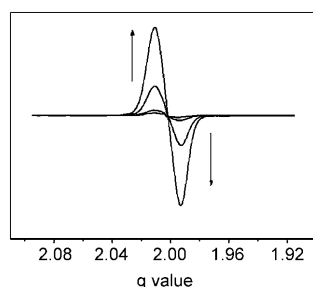


Figure 20. Detection of [3][•] with EPR spectroscopy in the initial stages of oxygenation of K[3] to **5**. Conditions: *T* = 20 K, freq. = 9.3826 GHz, att. = 30 dB, [Bu₄N]PF₆ (0.1 M) was added to the solution to obtain a better glass.

by O₂ likely produces the radical [3][•] and potassium superoxide (KO₂). These species could be kept close together by binding of the non-coordinated pyridine moiety of [3][•] to potassium, as in species **A** (Scheme 4). We propose that radical [3][•] reacts with O₂ or KO₂ to produce the ligand peroxo intermediate **C** in both cases. In the reaction with O₂, this probably involves a radical chain (auto-oxidation) pathway in which one-electron reduction of the intermediate ligand superoxo intermediate **B** by another molecule [3][•] produces **C** and regenerates a new species [3][•]. Collapse of the [3][•]···K⁺···O₂^{•−} radical pair **A** is an alternative direct route to species **C**. Extrusion of KOH from the ligand peroxide intermediate **C**, which is likely stabilised by binding of the peroxo oxygen(s) to K⁺, then produces **5** (see Scheme 4).

Since we did not detect any superoxide signals in the EPR spectra, their concentration must be very low. This could mean that either: i) direct collapse of the two radicals in **A** to form **C** is extremely fast, or ii) oxidation of [3][•] by O₂ is slow, but followed by a comparatively rapid decomposition of the thus formed superoxide. In the first case we only detect the slower detour radical chain pathway with EPR. In the case ii) the radical chain pathway is the only route to **5**, as the overall fast oxidation requires the presence of [3][•] in catalytic amounts. This conveniently explains the build-up of [3][•] revealed by EPR (without detectable superoxide) which slowly disappears towards the end of the reaction. The direct collapse of intermediate **A** to **C** cannot be excluded, though.

Conclusion

Deprotonation of [Ir(bpa)(cod)]⁺ ([1]⁺) produces the mono-deprotonated neutral amido complex [Ir(bpa–H)(cod)] (**2**), which can be further deprotonated to produce the anionic [Ir(bpa–2H)(cod)][−] species [3][−]. Complex [3][−] is best described as a 2e reduced redox form of the cationic imine complex [Ir^I(cod)(py–CH₂–N=CH–py)]⁺ ([3]⁺). The metal chelate ring of [3][−] and its rhodium analogue [4][−] appear to have a certain degree of aromaticity, which may explain their relatively facile formation. One-electron oxidation of [3][−] and [4][−] by Ag⁺ produces the neutral ligand radical complexes [3][•] and [4][•]. Oxygenation of K[3] with O₂ produces the neutral carboxamido complex [Ir(bpam–H)(cod)] (**5**). In this mono-oxygenation reaction ligand radical complex [3][•] is a clearly detectable intermediate. This sequence of deprotonation, oxidation and mono-oxygenation reactions clearly demonstrates the chemical “non-innocence” of bpa, which is noteworthy because bpa is generally considered to be a stable, robust and non-reactive ligand in coordination and organometallic chemistry.

Experimental Section

General methods: All procedures were performed under an argon or N₂ atmosphere, using standard Schlenk techniques. Solvents were dried and

distilled under argon before use by standard methods.^[25] NMR experiments were carried out on a Bruker AV 400 (400 MHz and 100 MHz for ¹H and ¹³C, respectively) and Bruker AV 500 (500 MHz and 125 MHz for ¹H and ¹³C, respectively). Chemical shifts are reported in ppm and referenced to SiMe₄, using the internal signal of the deuterated solvent as a reference. The bpa numbering for all the complexes is shown in Figure 9 for **2**, where Py-B represents the pyridyl coordinated to the iridium while Py-A represents the uncoordinated pyridine. The complexes $[\text{Ir}(\mu\text{-OMe})(\text{cod})_2]$,^[23] $[\text{Ir}(\text{bpa})(\text{cod})]\text{PF}_6$ (**[1]⁺**)^[23] and $[\text{Rh}(\text{bpa})(\text{cod})]\text{PF}_6$,^[8] as well as *N*-(2-picolyl)picolinamide (bpam)^[24] were prepared according to the literature descriptions. All other chemicals are commercially available and were used without further purification.

Syntheses of the complexes

[Ir(bpa-H)(cod)] (2): A suspension of $[\text{Ir}(\mu\text{-OMe})(\text{cod})_2]$ (200 mg, 0.30 mmol) in diethyl ether (20 mL) was slowly added to a solution of bis(picolyl)amine (bpa) (112 µL, 0.60 mmol) in diethyl ether (4 mL). An immediate red solution was formed after mixing the reagents. The solution was evaporated to ca. 5 mL and kept undisturbed at -20 °C overnight to render dark-red crystals, which were washed with cold hexane (3 × 3 mL) and vacuum-dried (233 mg, 78 %). ¹H NMR (500 MHz, [D₈]toluene, -40 °C): δ = 8.35 (d, *J* = 3.9 Hz, 1H, H^{A1}), 7.58 (d, *J* = 7.8 Hz, 1H, H^{A4}), 7.34 (d, *J* = 5.6 Hz, 1H, H^{B1}), 6.85 (td, *J* = 7.6, 1.7 Hz, 1H, H^{A3}), 6.37 (t, *J* = 6.1 Hz, 1H, H^{A2}), 6.32 (t, *J* = 7.3 Hz, 1H, H^{B3}), 6.10 (d, *J* = 7.8 Hz, 1H, H^{B4}), 5.82 (d, *J* = 6.3 Hz, 1H, H^{B2}), 4.56 (s, 1H) and 3.91 (s, 1H), CH₂ bpa, 3.63 (m, 2H), 2.67 (m, 2H), HC=(cod), 2.32 (m, 2H), 2.17 (m, 2H), CH₂^{exo} (cod), 1.73 (m, 2H), 1.63 ppm (m, 2H), CH₂^{endo} (cod); ¹³C{¹H} NMR (125 MHz, [D₈]toluene, -40 °C): δ = 171.1 C^{A5}, 164.6 C^{B5}, 149.2 C^{A1}, 145.1 C^{B1}, 136.0 C^{A3}, 135.0 C^{B3}, 121.3 C^{B2}, 121.1 C^{A2}, 120.3 C^{A4}, 119.8 C^{B4}, 69.2/59.8 CH₂ bpa, 64.4/53.5 HC=(cod), 32.6/32.1 ppm CH₂ (cod); elemental analysis calcd (%) for C₂₀H₂₄N₃Ir (498.6): C 48.17, H 4.85, N 8.43; found: C 48.25, H 4.73, N 8.36.

K[Ir(bpa-2H)(cod)] (K[3]): A brown solution of [Ir(bpa-H)(cod)] (**2**) (75.0 mg, 0.15 mmol) in THF (4 mL) was treated with solid KOtBu (20.2 mg, 0.18 mmol). After stirring for 2 h at RT, the resulting red-brown solution was carefully layered with hexane (10 mL) and kept undisturbed at -20 °C for 3 d. The resulting brown-red crystals were separated by decantation, washed with cold diethyl ether (3 mL), then with hexane (2 × 3 mL) and vacuum-dried (40.2 mg, 49.5 %). ¹H NMR (400 MHz, [D₈]THF, -70 °C): δ = 8.63 (d, *J* = 4.0 Hz, 1H, H^{A1}), 7.87 (td, *J* = 7.3, 1.5 Hz, 1H, H^{A3}), 7.36 (m, H^{A2-A4}), 6.99 (d, *J* = 6.2 Hz, 1H, H^{B1}), 6.66 (d, *J* = 8.8 Hz, 1H, H^{B4}), 6.38 (s, 1H, N=CH), 5.77 (t, *J* = 7.3 Hz, 1H, H^{B3}), 4.98 (t, *J* = 6.2 Hz, 1H, H^{B2}), 4.91 (s, 2H, CH₂ bpa), 3.27 (m, 2H), 2.83 (m, 2H), HC=(cod), 2.35 (m, 2H), 2.24 (m, 2H), CH₂^{exo} (cod), 2.01 ppm (m, 4H) CH₂^{endo} (cod); ¹³C{¹H} NMR (100 MHz, [D₈]THF, -70 °C): δ = 163.6 C^{A5}, 146.2 C^{A1}, 140.1 C^{B1}, 134.4 C^{A3}, 134.4 C^{B5}, 119.6 C^{A4}, 118.9 C^{A2}, 118.1 C^{B4}, 117.2 N=CH, 113.1 C^{B3}, 94.9 C^{B2}, 56.7 CH₂ bpa, 48.8/46.0 HC=(cod), 30.9/30.7 ppm CH₂ (cod); elemental analysis calcd (%) for C₂₀H₂₃N₃IrK (536.7): C 44.76, H 4.32, N 7.83; found: C 44.69, H 4.22, N 7.77.

[K(cryptand)][Ir(bpa-2H)(cod)] (K*[3]): A brown solution of [Ir(bpa-H)(cod)] (**2**) (50.3 mg, 0.10 mmol) in THF (4 mL) was treated with solid KOtBu (13.6 mg, 0.12 mmol). After stirring for 2 h at room temperature, solid cryptand (4,7,13,16,21,24-hexaoxa-1,10-diazabicyclo-[8.8.8]hexacosane) (68.4 mg, 0.18 mmol) was added and the solution was stirred for 30 min. Slow diffusion with hexane (10 mL) at -20 °C for 3 d rendered red-brown microcrystals, which were decanted, washed with diethyl ether (3 mL) and vacuum-dried (80.5 mg, 87.4 %). ¹H NMR (400 MHz, [D₈]THF, 25 °C): δ = 8.28 (ddd, *J* = 4.7, 1.7, 0.7 Hz, 1H, H^{A1}), 7.41 (td, *J* = 7.7, 1.8 Hz, 1H, H^{A3}), 7.18 (d, *J* = 7.9 Hz, 1H, H^{A4}); 6.87 (ddd, *J* = 7.2, 5.0, 2.0 Hz, 1H, H^{A2}), 6.68 (d, *J* = 6.7 Hz, 1H, H^{B1}), 6.32 (d, *J* = 9.0 Hz, 1H, H^{B4}), 6.09 (s, 1H, N=CH), 5.31 (ddd, *J* = 9.0, 5.5, 0.9 Hz, 1H, H^{B3}), 4.59 (s, 2H, CH₂ bpa), 4.55 (ddd, *J* = 6.8, 5.5, 1.3 Hz, 1H, H^{B2}), 2.89 (m, 2H) and 2.49 (m, 2H), HC=(cod), 2.08 (m, 2H)/1.94 (m, 2H), CH₂^{exo} (cod), 1.96 (m, 2H)/1.63 ppm (m, 2H) CH₂^{endo} (cod); ¹³C{¹H} NMR (100 MHz, [D₈]THF, 25 °C): δ = 168.3 C^{A5}, 148.1 C^{A1}, 143.4 C^{B1}, 137.7 C^{B5}, 136.2 C^{A3}, 122.8 C^{A4}, 121.6 C^{B4}, 120.9 N=CH, 120.7 C^{A2}, 114.7 C^{B3}, 96.6 C^{B2}, 60.7 CH₂ bpa, 51.0/48.3 HC=(cod), 33.84/33.81 ppm CH₂

(cod); elemental analysis calcd (%) for C₃₈H₅₉N₃O₆IrK (913.2): C 49.98, H 6.51, N 7.67; found: C 50.01, H 6.63, N 7.63.

K[Rh(bpa-2H)(cod)] (K[4]): A NMR tube was charged with solid [Rh(bpa)(cod)]Cl (20 mg, 0.044 mmol) and KOtBu (15.1 mg, 0.135 mmol) and then [D₈]THF (0.5 mL) were added under a rigorous argon atmosphere. An immediate dark-brown solution was formed. ¹H NMR (400 MHz, [D₈]THF, -70 °C): δ = 8.36 (dd, *J* = 5.2, 1.5 Hz, 1H, H^{A1}), 7.61 (td, *J* = 7.7, 1.6 Hz, 1H, H^{A3}), 7.06 (m, H^{A2-A4}), 6.39 (d, *J* = 6.7 Hz, 1H, H^{B1}), 6.13 (d, *J* = 9.1 Hz, 1H, H^{B4}), 5.55 (s, 1H, N=CH), 5.33 (dd, *J* = 9.0, 5.5 Hz, 1H, H^{B3}), 4.49 (t, *J* = 5.7 Hz, 1H, H^{B2}), 4.38 (s, 2H, CH₂ bpa), 3.39 (m, 2H), 2.94 (m, 2H), HC=(cod), 2.75 (m, 2H), 2.15 (m, 2H), CH₂^{exo} (cod), 1.88 ppm (m, 4H) CH₂^{endo} (cod); ¹³C{¹H} NMR (100 MHz, [D₈]THF, -40 °C): δ = 167.6 C^{A5}, 149.4 C^{A1}, 144.3 C^{B1}, 137.0 C^{A3}, 134.7 C^{B5}, 122.7 C^{A4}, 121.6 C^{B4}, 120.9 N=CH, 117.3 C^{A2}, 116.1 C^{B3}, 95.7 C^{B2}, 59.7 CH₂ bpa, 69.3 (d, *J*(C,Rh) = 12.4 Hz)/59.7 (d, *J*(C,Rh) = 12.7 Hz) HC=(cod), 32.8/32.5 ppm CH₂ (cod).

[Ir(bpam-H)(cod)] (5): Solid *N*-(2-picolyl)picolinamide (bpam) (134.3 mg, 0.63 mmol) was added to a solution of $[\text{Ir}(\mu\text{-OMe})(\text{cod})_2]$ (205.2, 0.31 mmol) in dichloromethane (5 mL). An immediate red solution was formed after mixing the reagents. The solution was evaporated to ca. 2 mL, layered with hexane (10 mL) and kept undisturbed at -20 °C overnight to render red crystals, which were washed with cold hexane (3 × 3 mL) and vacuum-dried (292.4 mg, 92 %). ¹H NMR (400 MHz, C₆D₆, 25 °C): δ = 8.51 (ddd, *J* = 4.7, 1.6, 0.8 Hz, 1H, H^{A1}), 7.95 (ddd, *J* = 7.8, 1.5, 0.6 Hz, 1H, H^{B4}), 7.77 (d, *J* = 7.9 Hz, 1H, H^{A4}), 7.15 (m, 2H, H^{B1-A3}), 6.80 (td, *J* = 7.7, 1.5 Hz, 1H, H^{B3}), 6.60 (ddd, *J* = 7.4, 4.9, 0.9 Hz, 1H, H^{A2}), 6.21 (ddd, *J* = 7.3, 5.5, 1.5 Hz, 1H, H^{B2}), 5.17 (s, 2H, CH₂^{bpam}), 4.39 (m, 2H), 3.21 (m, 2H), HC=(cod), 2.17 (m, 4H, CH₂^{exo} (cod)), 1.59 ppm (m, 4H, CH₂^{endo} (cod)); ¹³C{¹H} NMR (100 MHz, C₆D₆, 25 °C): δ = 176.3 CO, 162.5 C^{A5}, 153.6 C^{B5}, 149.1 C^{A1}, 144.4 C^{B1}, 139.6 C^{B3}, 135.8 C^{A3}, 126.1 C^{B2}, 125.4 C^{B4}, 122.2 C^{A4}, 121.2 C^{A2}, 69.5/59.6 HC=(cod), 51.1 CH₂^{bpam}, 32.3/31.2 ppm CH₂ (cod); elemental analysis calcd (%) for C₂₀H₂₂N₃OIr (512.6): C 46.86, H 4.32, N 8.20; found: C 46.82, H 4.21, N 8.15.

EPR spectroscopy: Experimental X-band EPR spectra were recorded on a Bruker EMX Plus spectrometer. A Q-band pulsed ENDOR spectrum in the range of ¹H couplings were recorded on a Bruker Elexsys E-580 FT EPR Q-band spectrometer. We thank Professor F. Neese (Universität Bonn) for a copy of his EPR simulation program.

Electrochemistry: Analytical-grade tetrahydrofuran (THF), purchased from Acros Chimica, was dried by a conventional procedure^[25] and freshly distilled prior to use. The supporting electrolyte Bu₄NPF₆ (Aldrich) was recrystallised twice from absolute ethanol and dried under vacuum at 80 °C for 3 days. Cyclic voltammograms of **K[3]** were recorded with an EG&G PAR Model 283 potentiostat, using an air-tight single-compartment three-electrode cell placed in a Faraday cage. The cell contained a platinum disk working electrode (apparent surface area of 0.42 mm², polished carefully with a 0.25 µm diamond paste (Oberflächentechnologien Ziesmer, Kempen, Germany)), a platinum wire auxiliary electrode and a silver wire pseudoreference electrode. The standard^[26] ferrocene/ferrocenium (Fc/Fc⁺) redox couple served as an internal reference system. The Fc/Fc⁺ couple occurs at 0.53 V vs. SCE in THF.^[27]

Spectroelectrochemistry: UV/Vis spectral changes during oxidation of **[3]⁻** were monitored with an optically transparent thin-layer electrochemical (OTTLE) cell^[28] equipped with Pt minigrad working electrodes and CaF₂ windows. The potential of the working electrode was controlled by a PA4 (EKOM, Polná, Czech Republic) potentiostat. The OTTLE cell was positioned in the sample compartment of a Hewlett Packard 8453 diode-array spectrophotometer.

DFT geometry optimisations and spectral property calculations: The geometry optimisations of the complexes **[3]⁻**, **[3]⁺**, **[4]⁻**, **[3][•]** and **[4][•]** were carried out with the Turbomole program^[29a,b] coupled to the PQS Baker optimiser.^[30] Geometries were fully optimised as minima at the bp86^[31] level using the Turbomole SV(P) basis set^[29c,d] on all atoms and also at the B3LYP level^[32] using the polarised triple-ζ TZVP basis^[29c,f] (small-core pseudopotential^[29c,e] on Rh or Ir). In the latter case also a single point cosmo solvent correction (ε = 7.52) was applied.^[33] Orbitals and spin densities were visualised with the Molden program.^[34] The EPR parameters^[35] of **[3][•]** and **[4][•]** were calculated with the ADF^[36] program

system using the BP86^[31] functional with the ZORA/TZP basis sets supplied with the program (all electron, core double- ζ , valence triple- ζ polarised basis set on all atoms), using the coordinates from the structures optimised in Turbomole (BP86, SV(P)) as input.

Low-lying excitations were calculated by time-dependent DFT (TD-DFT) at the optimised ground-state geometry using Gaussian 03^[37] program package. Calculations employed the Perdew, Burke, Ernzerhof exchange and correlation functional (PBE0).^[38] The solvent influence was described by the polarisable conductor calculation model (CPCM).^[39] The UKS approach was used for calculations on radical [3]. In TD-DFT quasi-relativistic effective core pseudopotentials and corresponding optimised set of basis functions for Ir^[40] were used together with cc-pvdz correlation consistent polarised valence double- ζ basis set^[40] for remaining atoms.

X-ray diffraction studies on complexes 2, K*[3]·C₄H₈O and 5: Intensity measurements were collected with a Smart Apex diffractometer, with graphite-monochromated MoK α radiation. A semiempirical absorption correction was applied to each data set, with the multi-scan^[41] methods. Selected crystallographic data can be found in Table 4. The structures were solved by the Patterson method and refined by full-matrix least-squares, with the program SHELXL^[42] in the WINGX^[43] package.

CCDC 725974, 725975 and 725976 contain the supplementary crystallographic data for this paper. These data can be obtained free of charge from The Cambridge Crystallographic Data Centre via www.ccdc.cam.ac.uk/data_request/cif

Table 4. Selected crystal, measurement and refinement data for compounds 2, K*[3]·C₄H₈O and 5.

	2	K*[3]·C ₄ H ₈ O	5
formula	C ₂₀ H ₂₄ IrN ₃	C ₃₈ H ₅₉ Ir K N ₅ O ₆ ·C ₄ H ₈ O	C ₂₀ H ₂₂ Ir N ₃ O
formula weight	498.62	985.31	512.61
colour	orange-brown	dark-red	red
crystal system	monoclinic	monoclinic	monoclinic
space group	<i>P</i> 2 ₁ / <i>c</i>	<i>P</i> 2 ₁ / <i>c</i>	<i>P</i> 2 ₁ / <i>n</i>
<i>a</i> [Å]	13.2102(18)	14.480(3)	18.0944(18)
<i>b</i> [Å]	7.2978(10)	23.954(5)	10.1833(10)
<i>c</i> [Å]	18.503(3)	12.974(3)	18.7806(18)
α [°]	90.00	90.00	90.00
β [°]	106.165(2)	102.977(3)	100.918(2)
γ [°]	90.00	90.00	90.00
<i>V</i> [Å ³]	1713.2(4)	4385.1(15)	3397.9(6)
<i>Z</i>	4	4	8
<i>F</i> (000)	968	2024	1984
ρ_{calcd} [g cm ⁻³]	1.933	1.492	2.004
μ [mm ⁻¹]	7.799	3.193	7.872
crystal size [mm]	0.19, 0.07, 0.06	0.14, 0.09, 0.03	0.17, 0.14, 0.06
<i>T</i> [K]	100(2)	100(2)	100(2)
θ limits [°]	1.60, 28.24	1.67, 25.16	1.74, 28.28
collected reflns.	20 466	31 690	22 245
unique reflns.	4145	7853 (0.0981)	8105 (0.0409)
(<i>R</i> _{int})	(0.0509)		
reflns. with <i>I</i> > 2 σ (<i>I</i>)	2841	5925	7293
parameters/restraints	217/0	494/26	448/0
<i>R</i> ₁ (on <i>F</i> , <i>I</i> > 2 σ (<i>I</i>))	0.0353	0.0698	0.0276
<i>wR</i> ₂ (on <i>F</i> ² , all data)	0.0847	0.1355	0.0599
max./min. $\Delta\rho$ [e Å ⁻³]	2.074/−1.980	1.756/−2.845	1.386/−0.962
goodness of fit	1.055	1.124	1.057

Acknowledgements

This research was supported by the Netherlands Organization for Scientific Research (NWO-CW), the European Research Council (ERC, EU 7th framework program) Grant Agreement 202886-CatCIR, the MEC/FEDER (Project CTQ2008-03860, Spain) and GA (Project PI55/08, Spain), the Grant Agency of the Academy of Sciences of the Czech Republic (S.Z., Grant KAN100400702), the Ministry of Education of the Czech Republic (S.Z., Grant OC 139), the Radboud University Nijmegen and the University of Amsterdam. P.d.R. thanks GA for a fellowship.

- a) D. G. H. Hetterscheid, B. de Bruin, *Eur. J. Inorg. Chem.* **2007**, 211–230; b) “The Organometallic Chemistry of Rh, Ir, Pd and Pt Based Radicals; Higher Valent Species”: B. de Bruin, D. G. H. Hetterscheid, A. J. J. Koekoek, H. Grützmacher, *Prog. Inorg. Chem.* **2007**, 55, Chapter 5.
- a) C. G. Pierpont, C. W. Lange, *Prog. Inorg. Chem.* **1994**, 41, 331–442; b) C. G. Pierpont, A. S. Attia, *Collect. Czech. Chem. Commun.* **2001**, 66, 33–51; c) H. Chun, C. N. Verani, P. Chaudhuri, E. Bothe, E. Bill, T. Weyhermüller, K. Wieghardt, *Inorg. Chem.* **2001**, 40, 4157–4166; d) P. Chaudhuri, C. N. Verani, E. Bill, E. Bothe, T. Weyhermüller, K. Wieghardt, *J. Am. Chem. Soc.* **2001**, 123, 2213–2223; e) D. Herebian, P. Ghosh, H. Chun, E. Bothe, T. Weyhermüller, K. Wieghardt, *Eur. J. Inorg. Chem.* **2002**, 1957–1967; f) D. N. Hendrickson, C. G. Pierpont, *Top. Curr. Chem.* **2004**, 234, 63–95; g) C. W. Lange, C. G. Pierpont, *J. Am. Chem. Soc.* **1992**, 114, 6582–6583.
- a) B. de Bruin, E. Bill, E. Bothe, T. Weyhermüller, K. Wieghardt, *Inorg. Chem.* **2000**, 39, 2936–2947; b) P. H. M. Budzelaar, B. de Bruin, A. W. Gal, K. Wieghardt, J. H. van Lenthe, *Inorg. Chem.* **2001**, 40, 4649–4655; c) D. Enright, S. Gambarotta, G. P. A. Yap, P. H. M. Budzelaar, *Angew. Chem.* **2002**, 114, 4029–4032; *Angew. Chem. Int. Ed.* **2002**, 41, 3873–3876; d) I. Sugiyama, I. Korobkov, S. Gambarotta, A. Mueller, P. H. M. Budzelaar, *Inorg. Chem.* **2004**, 43, 5771–5779; e) J. Scott, S. Gambarotta, I. Korobkov, Q. Knijnenburg, B. de Bruin, P. H. M. Budzelaar, *J. Am. Chem. Soc.* **2005**, 127, 17204–17206; f) T. M. Kooistra, D. G. H. Hetterscheid, E. Schwartz, Q. Knijnenburg, P. H. M. Budzelaar, A. W. Gal, *Inorg. Chim. Acta* **2004**, 357, 2945–2952; g) Q. Knijnenburg, A. D. Horton, H. van der Heijden, T. M. Kooistra, D. G. H. Hetterscheid, J. M. M. Smits, B. de Bruin, P. H. M. Budzelaar, A. W. Gal, *J. Mol. Catal. A* **2005**, 232, 151–159.
- D. G. H. Hetterscheid, J. Kaiser, E. Reijerse, T. P. J. Peters, S. Theissen, A. N. J. Blok, J. M. M. Smits, R. de Gelder, B. de Bruin, *J. Am. Chem. Soc.* **2005**, 127, 1895–1905.
- a) T. Buttner, J. Geier, G. Frison, J. Harmer, C. Calle, A. Schweiger, H. Schönberg, H. Grützmacher, *Science* **2005**, 307, 235–238; b) P. Maire, M. Königsmann, A. Sreekanth, J. Harmer, A. Schweiger, H. Grützmacher, *J. Am. Chem. Soc.* **2006**, 128, 6578–6580.
- a) D. G. H. Hetterscheid, B. de Bruin, *Chem. Eur. J.* **2007**, 13, 3386–3405; b) B. B. Wayland, A. E. Sherry, A. G. Bunn, *J. Am. Chem. Soc.* **1993**, 115, 7675–7684.
- M. Königsmann, N. Donati, D. Stein, H. Schönberg, J. Harmer, A. Sreekanth, H. Grützmacher, *Angew. Chem.* **2007**, 119, 3637–3640; *Angew. Chem. Int. Ed.* **2007**, 46, 3567–3570.
- D. G. H. Hetterscheid, B. de Bruin, J. M. M. Smits, A. W. Gal, *Organometallics* **2003**, 22, 3022–3024.
- A. Friedrich, R. Ghosh, R. Kolb, E. Herdtweck, S. Schneider, *Organometallics* **2009**, 28, 708–718, and references therein.
- H. W. Roesky, M. Andruh, *Coord. Chem. Rev.* **2003**, 236, 91–119.
- S. Grimme, *Angew. Chem.* **2008**, 120, 3478–3483; *Angew. Chem. Int. Ed.* **2008**, 47, 3430–3434.
- C. Tejel, M. A. Ciriano, M. P. del Rio, D. G. H. Hetterscheid, N. Tsi-chilis i Spitas, J. M. M. Smits, B. de Bruin, *Chem. Eur. J.* **2008**, 14, 10932–10936.
- a) C. C. Lu, E. Bill, T. Weyhermüller, E. Bothe, K. Wieghardt, *J. Am. Chem. Soc.* **2008**, 130, 3181–3197; b) M. van Gastel, C. C. Lu, K. Wieghardt, W. Lubitz, *Inorg. Chem.* **2009**, 48, 2626–2632; c) M. M. Khusniyarov, T. Wehermüller, E. Bill, K. Wieghardt, *J.*

- Am. Chem. Soc.* **2009**, *131*, 1208–1221; d) M. Ghosh, S. Sproules, T. Wehermüller, K. Wieghardt, *Inorg. Chem.* **2008**, *47*, 5963–5970; e) N. Muresan, C. C. Lu, M. Ghosh, J. C. Peters, M. Abe, L. M. Henling, T. Wehermüller, E. Bill, K. Wieghardt, *Inorg. Chem.* **2008**, *47*, 4579–4590; f) M. Ghosh, T. Wehermüller, K. Wieghardt, *Dalton Trans.* **2008**, 5149–5151.
- [14] Attempts to prepare complex $[3]^+$ from the imine ligand $\text{py-CH}_2\text{-N=CH-py}$ and $[\text{Ir}(\text{cod})(\text{NCMe})_2](\text{BF}_4)$ failed, in good agreement with the irreversible oxidation from $[3]^-$ to $[3]^+$ in the cyclic voltammogram: see reference [19].
- [15] a) S. W. Kohl, L. Weiner, L. Schwartzburd, L. Konstantinovskii, L. J. W. Shimon, Y. Ben-David, M. A. Iron, D. Milstein, *Science* **2009**, *324*, 74; b) C. Gunanathan, Y. Ben-David, D. Milstein, *Science* **2007**, *317*, 790; c) J. Zhang, G. Leituss, Y. Ben-David, D. Milstein, *J. Am. Chem. Soc.* **2005**, *127*, 10840; d) J. Zhang, G. Leituss, Y. Ben-David, D. Milstein, *Angew. Chem.* **2006**, *118*, 1131; *Angew. Chem. Int. Ed.* **2006**, *45*, 1113; e) T. Schaub, U. Radius, Y. Diskin-Posner, G. Leituss, L. J. W. Shimon, D. Milstein, *Organometallics* **2008**, *27*, 1892–1901; f) E. Ben-Ari, G. Leituss, L. J. W. Shimon, D. Milstein, *J. Am. Chem. Soc.* **2006**, *128*, 15390–15391.
- [16] See for example: a) M. Bikrani, M. A. Garralda, L. Ibarlucea, E. Pinella, *J. Organomet. Chem.* **1995**, *489*, 93–99; b) F. C. Anson, T. J. Collins, R. J. Coots, S. L. Gipson, T. E. Krafft, B. D. Santarsiero, G. H. Spies, *Inorg. Chem.* **1987**, *26*, 1161–1168; c) E. Rijnberg, B. Richter, K.-H. Thiele, J. Boersma, N. Veldman, A. L. Spek, G. van Koten, *Inorg. Chem.* **1998**, *37*, 56–63; d) E. Rijnberg, J. Boersma, T. B. H. Jastrzebski, M. T. Lakin, A. L. Spek, G. van Koten, *Organometallics* **1997**, *16*, 3158–3164.
- [17] a) P. S. Braterman, J.-I. Song, C. Vogler, W. Kaim, *Inorg. Chem.* **1992**, *31*, 222–224; b) C. Vogler, B. Schwederski, A. Klein, W. Kaim, *J. Organomet. Chem.* **1992**, *436*, 367–378; c) A. Klein, W. Kaim, *Organometallics* **1995**, *14*, 1176–1186; d) A. Klein, H.-D. Hausen, W. Kaim, *J. Organomet. Chem.* **1992**, *440*, 207–217; e) A. Klein, W. Kaim, E. Waldhör, H.-D. Hausen, *J. Chem. Soc. Perkin Trans. 2* **1995**, 2121–2126; f) A. Klein, E. J. L. McInnes, W. Kaim, *J. Chem. Soc. Dalton Trans.* **2002**, 2371–2378.
- [18] a) W. Kaim, A. Klein, S. Hasenzahl, H. Stoll, S. Zális, J. Fiedler, *Organometallics* **1998**, *17*, 237–247; b) S. Hasenzahl, H.-D. Hausen, W. Kaim, *Chem. Eur. J.* **1995**, *1*, 95–99; c) A. Klein, S. Hasenzahl, W. Kaim, *J. Chem. Soc. Perkin Trans. 2* **1997**, 2573–2578.
- [19] a) W. Kaim, R. Reinhardt, S. Greulich, J. Fiedler, *Organometallics* **2003**, *22*, 2240–2244; b) O. Heilmann, F. M. Hornung, W. Kaim, J. Fiedler, *J. Chem. Soc. Faraday Trans.* **1996**, *92*, 4233–4238; c) O. Heilmann, F. M. Hornung, J. Fiedler, W. Kaim, *J. Organomet. Chem.* **1999**, *589*, 2–10; d) M. Sieger, W. Kaim, D. J. Stufkens, T. L. Snoeck, H. Stoll, S. Zális, *Dalton Trans.* **2004**, 3815–3821.
- [20] F. Hartl, P. Rosa, L. Ricard, P. Le Floch, S. Zális, *Coord. Chem. Rev.* **2007**, *251*, 557–576.
- [21] Subsequent oxidation of $[3]^-$ to $[3]^+$ was observed as an totally irreversible anodic wave at $E_{\text{pa}} = 0.10$ V versus Fc/Fc^+ (THF, 100 mV s^{-1}).
- [22] a) C. Tejel, M. A. Ciriano, *Top. Organomet. Chem.* **2007**, *22*, 97–124; b) B. de Bruin, P. H. M. Budzelaar, A. W. Gal, *Angew. Chem.* **2004**, *116*, 4236–4251; *Angew. Chem. Int. Ed.* **2004**, *43*, 4142–4157.
- [23] R. Usón, L. A. Oro, J. A. Cabeza, *Inorg. Synth.* **1985**, *23*, 126–129.
- [24] J. M. Rowland, M. M. Olmstead, P. K. Mascharak, *Inorg. Chem.* **2002**, *41*, 2754–2760.
- [25] D. D. Perrin, W. L. F. Armarego, *Purification of Laboratory Chemicals*, 3rd ed., Pergamon Press, Exeter, **1988**.
- [26] G. Gritzner, J. Kúta, *Pure Appl. Chem.* **1984**, *56*, 461–466.
- [27] S. J. Borg, S. P. Best, *J. Electroanal. Chem.* **2002**, *535*, 57–64.
- [28] M. Krejčík, M. Daněk, F. Hartl, *J. Electroanal. Chem. Interfacial Electrochem.* **1991**, *317*, 179–187.
- [29] a) Turbomole Version 5, R. Ahlrichs, M. Bär, H.-P. Baron, R. Bauernschmitt, S. Böcker, M. Ehrig, K. Eichkorn, S. Elliott, F. Furche, F. Haase, M. Häser, C. Hättig, H. Horn, C. Huber, U. Huniar, M. Kattannek, A. Köhn, C. Kölmel, M. Kollwitz, K. May, C. Ochsenfeld, H. Öhm, A. Schäfer, U. Schneider, O. Treutler, K. Tsereteli, B. Unterreiner, M. von Arnim, F. Weigend, P. Weis, H. Weiss, University of Karlsruhe, Karlsruhe, **2002**; b) O. Treutler, R. Ahlrichs, *J. Chem. Phys.* **1995**, *102*, 346–354; c) Turbomole basis set library, Turbomole Version 5, see reference [29a]; d) A. Schäfer, H. Horn, R. Ahlrichs, *J. Chem. Phys.* **1992**, *97*, 2571–2577; e) D. Andrae, U. Haeussermann, M. Dolg, H. Stoll, H. Preuss, *Theor. Chim. Acta* **1990**, *77*, 123–141; f) A. Schäfer, C. Huber, R. Ahlrichs, *J. Chem. Phys.* **1994**, *100*, 5829–5835; g) R. Ahlrichs, K. May, *Phys. Chem. Chem. Phys.* **2000**, *2*, 943–945.
- [30] a) PQS Version 2.4, Parallel Quantum Solutions, Fayetteville, Arkansas, **2001** (the Baker optimizer is available separately from PQS upon request); b) J. Baker, *J. Comput. Chem.* **1986**, *7*, 385–395.
- [31] a) A. D. Becke, *Phys. Rev. A* **1988**, *38*, 3098–3100; b) J. P. Perdew, *Phys. Rev. B* **1986**, *33*, 8822–8824.
- [32] a) C. Lee, W. Yang, R. G. Parr, *Phys. Rev. B* **1988**, *37*, 785–789; b) A. D. Becke, *J. Chem. Phys.* **1993**, *98*, 1372–1377; c) A. D. Becke, *J. Chem. Phys.* **1993**, *98*, 5648–5652; d) Calculations were performed using the Turbomole functional “B3LYP”, which is not identical to the Gaussian “B3LYP” functional.
- [33] A. Klamt, G. Schürmann, *J. Chem. Soc. Perkin Trans. 2* **1993**, 799–805.
- [34] “Molden: a pre- and post-processing program for molecular and electronic structures”: G. Schaftenaar, J. H. Noordik, *J. Comput.-Aided Mol. Des.* **2000**, *14*, 123–134.
- [35] Some references and reviews on DFT approaches to EPR parameters: a) E. van Lenthe, A. van der Avoird, P. E. S. Wormer, *J. Chem. Phys.* **1997**, *107*, 2488–2498; b) E. van Lenthe, A. van der Avoird, P. E. S. Wormer, *J. Chem. Phys.* **1998**, *108*, 4783–4796; c) F. Neese, *Curr. Opin. Chem. Biol.* **2003**, *7*, 125–135; d) F. Neese, E. Solomon, *Magnetochemistry—From Molecules to materials* (Eds.: J. S. Miller, M. Drillon), Wiley, New York, **2003**, p. 345–466; e) G. Peng, J. Nichols, E. A. McCullough, J. Spence, *Inorg. Chem.* **1994**, *33*, 2857–2864.
- [36] ADF2006: a) E. J. Baerends, D. E. Ellis, P. Ros, *Chem. Phys.* **1973**, *2*, 41–51; b) L. Versluis, T. Ziegler, *J. Chem. Phys.* **1988**, *88*, 322–328; c) G. te Velde, E. J. Baerends, *J. Comput. Phys.* **1992**, *99*, 84–98; d) C. Fonseca Guerra, J. G. Snijders, G. te Velde, E. J. Baerends, *Theor. Chem. Acc.* **1998**, *99*, 391–403.
- [37] Gaussian 03, Revision C.02, M. J. Frisch, G. W. Trucks, H. B. Schlegel, G. E. Scuseria, M. A. Robb, J. R. Cheeseman, J. A. Montgomery, Jr., T. Vreven, K. N. Kudin, J. C. Burant, J. M. Millam, S. S. Iyengar, J. Tomasi, V. Barone, B. Mennucci, M. Cossi, G. Scalmani, N. Rega, G. A. Petersson, H. Nakatsuji, M. Hada, M. Ehara, K. Toyota, R. Fukuda, J. Hasegawa, M. Ishida, T. Nakajima, Y. Honda, O. Kitao, H. Nakai, M. Klene, X. Li, J. E. Knox, H. P. Hratchian, J. B. Cross, V. Bakken, C. Adamo, J. Jaramillo, R. Gomperts, R. E. Stratmann, O. Yazyev, A. J. Austin, R. Cammi, C. Pomelli, J. W. Ochterski, P. Y. Ayala, K. Morokuma, G. A. Voth, P. Salvador, J. J. Dannenberg, V. G. Zakrzewski, S. Dapprich, A. D. Daniels, M. C. Strain, O. Farkas, D. K. Malick, A. D. Rabuck, K. Raghavachari, J. B. Foresman, J. V. Ortiz, Q. Cui, A. G. Baboul, S. Clifford, J. Cioslowski, B. B. Stefanov, G. Liu, A. Liashenko, P. Piskorz, I. Komaromi, R. L. Martin, D. J. Fox, T. Keith, M. A. Al-Laham, C. Y. Peng, A. Nanayakkara, M. Challacombe, P. M. W. Gill, B. Johnson, W. Chen, M. W. Wong, C. Gonzalez, J. A. Pople, Gaussian, Inc., Wallingford CT, **2004**.
- [38] J. P. Perdew, K. Burke, M. Ernzerhof, *Phys. Rev. Lett.* **1996**, *77*, 3865–3868.
- [39] M. Cossi, N. Rega, G. Scalmani, V. Barone, *J. Comput. Chem.* **2003**, *24*, 669–681.
- [40] D. E. Woon, T. H. Dunning, Jr., *J. Chem. Phys.* **1993**, *98*, 1358–1371.
- [41] SADABS, G. M. Sheldrick, Bruker AXS, Madison, **1997**.
- [42] SHELXL-97: Program for Crystal Structure Refinement, G. M. Sheldrick, University of Göttingen, Göttingen (Germany), **1997**.
- [43] L. F. Farrugia, *J. Appl. Crystallogr.* **1999**, *32*, 837–838.

Received: April 17, 2009
Published online: September 29, 2009